International Journal of Thermal Sciences 49 (2010) 59–66

Contents lists available at ScienceDirect

International Journal of Thermal Sciences

journal homepage: www.elsevier.com/locate/ijts

On the evaporation rate of ultra-thin liquid film at the nanostructured surface: A molecular dynamics study

Gyoko Nagayama*, Masako Kawagoe, Atsushi Tokunaga, Takaharu Tsuruta

Department of Mechanical Engineering, Kyushu Institute of Technology, Sensui 1-1, Tobata, Kitakyushu 805-8550, Japan

ARTICLE INFO

Article history:
Received 13 January 2008
Received in revised form
1 June 2009
Accepted 3 June 2009
Available online 8 July 2009

Keywords:
Evaporation rate
Ultra-thin liquid film
Nanostructured surface
Molecular dynamics simulation
Interface thermal resistance

ABSTRACT

Molecular dynamic (MD) simulations have been carried out to study the effect of the nanostructures on the evaporation rate of the ultra-thin liquid film at the solid surface. Simple Lennard-Jones (LJ) fluids are simulated as the ultra-thin liquid film in the non-equilibrium simulation system. The liquid film is confined in a nanochannel composed of two solid surfaces designed with nanostructures in a shape of molecular-scale unevenness. The potential function between solid and liquid molecules is represented by a modified LJ function to conduct the solid–liquid interfaces of different surface wettability. For the steady non-equilibrium MD simulation, the liquid film is subjected to the steady heat flux passing through the nanostructured surfaces. It is found that the interface thermal resistance decreases at the nanostructured surface and apparent heat transfer enhancement is achieved due to the surface area increment. For the unsteady non-equilibrium MD simulation, the vapor has been sandwiched between the liquid films in contact with the nanostructured surfaces of high and low temperature respectively. It is found that the evaporation rate of the ultra-thin liquid film has a larger value than that of the flat surface when the film thickness is larger than that of the adsorbed layer.

1. Introduction

Recent progresses in ultra-fine manufacturing technology enable us to control surface structures in nanoscale and its application to microscale thermal manipulation have attracted a great deal of attention. Although a surface with nanoscale structures has the possibility of changing wettability at the solid–liquid interface [1–5] as well as the enhancement of heat transfer [6–8], in a macroscopic point of view, the nanostructured surface is a kind of ultra flat surface because its surface roughness is in nanoscale. However, the difference between the nanoscale and the conventional scale heat transfer mechanisms by its very nature has not been clarified yet. For the heat and mass transfer process in the region near the contact line during evaporation, as shown in Fig. 1, the traditional macroscopic description of an ultra-thin liquid film on a heated solid substrate based on the continuum assumption is open to question. With the decrease of the domain size of the liquid film, the interface resistances at the liquid–vapor interface and the solid–liquid interface become distinct and the understanding of the molecular interaction at the interface shows important.

Molecular dynamics (MD) simulation is a useful method to explore the nanoscale characteristics of the heat and mass transfer at the solid–liquid interface [9–14]. Previous study by Maruyama and Kimura [9] showed that the thermal resistance has a strong dependence on the solid–liquid surface wettability. Other works of the liquid film on the flat solid surface have been conducted by Yi et al. [10] and Ji et al. [11]. However, the evaporation rate of ultra-thin liquid film at the nanostructured surface has not been attracted much attention.

In this study, MD simulations have been carried out to study the effect of the nanostructures on the interface resistance as well as the evaporation rate of the ultra-thin liquid film at the solid surface. As far as we know, this is the first work concerning on the thin liquid film at the nanostructured solid surface.

2. Simulation method

MD simulations are performed for the liquid film confined in a nanochannel bounded by two planar solid walls [15,16]. As shown in Fig. 2, two kinds of simulation cell are prepared and both liquid films are subjected to a heat flow from a wall at high temperature $T = 120$ K to a wall at low temperature $T = 100$ K. The simulation cells have the same size in x and y direction of $Lx = 5.83$ nm, $Ly = 3.85$ nm, but differ in size in the z direction. For simulation cell (1), Lz is 7.22 nm and the distance separated between two planar

* Corresponding author. Tel./fax: +81 93 884 3139.
E-mail address: nagayama@mech.kyutech.ac.jp (G. Nagayama).

1290-0729/$ – see front matter © 2009 Elsevier Masson SAS. All rights reserved.
doi:10.1016/j.ijthermalsci.2009.06.001

Nomenclature

a	spacing between two nanostructures, nm
b	width of the nanostructure, nm
D	distance between two solid walls, nm
h	height of the nanostructure, nm
k_B	Boltzmann constant, $m^2\,kg\,s^{-2}\,K^{-1}$
m	mass transfer rate, $kg\,m^{-2}\,s^{-1}$
m_a	mass of an atom, kg
N	number of particles
P	pressure, Pa
q	heat flux, $W\,m^{-2}$
r	distance between pair particles, m
r_w	area ratio of nanostructured to flat surface, –
R_i	thermal resistance at solid–liquid interface, $m^2\,K\,W^{-1}$
s	size parameter being equal to $a+b$, nm
V	volume of the bin, m^3
$V_{n,i}$	velocity component i (=x,y,z) of atom n, $m\,s^{-1}$
$\overline{V}_i$	mean velocity component i (=x,y,z), $m\,s^{-1}$

Greek symbols

α	potential parameter, –
β	potential parameter, –
ε	energy parameter of potential function, J
ϕ	pair potential, J
λ	thermal conductivity, $W\,m^{-1}\,K^{-1}$
θ	contact angle, °
ρ	density, $kg\,m^{-3}$
σ	length parameter of potential function, m

Subscripts

C	cooling surface
H	heating surface
i	interface
l	liquid
s	solid
x	x direction
y	y direction
z	z direction
w	wall

walls D is 3.60–5.41 nm. In simulation cell (1), the nanochannel is filled with liquid near a saturation state and the thin liquid film is only subjected to a heat flow without phase change phenomena. Thus, a steady heat flux passing through the solid–liquid interface can be obtained. In simulation cell (2), Lz is enlarged to 12.62 nm and the nanochannel is filled with liquid and vapor. Since simulation cell (2) is subjected to the same heat flow as simulation cell (1), the liquid particles evaporate from the liquid–vapor interface upon the high temperature wall and condense at the liquid–vapor interface upon the low temperature wall. That is, simulation cell (2) subjects to the heat flow and the mass flux. The system of simulation cell (2) is in an unsteady state when phase change phenomena occur at the liquid–vapor interface. Since simulation cell (2) contains both the solid–liquid interface and the liquid–vapor interface, the total resistance of simulation cell (2) is larger than that of simulation cell (1) as a matter of course.

Periodic boundary conditions are applied along the x and y directions. In the z direction, outside each solid wall of the simulation cell, 4 layers of phantom solid atoms anchored by their lattice are located to model a semi-infinite potential field. For the sake of physical understanding, the solid walls are assumed to be made of platinum and the Lennard-Jones (LJ) fluid is argon. Each solid wall consisted of more than four layers of atoms arranged as a FCC lattice and its ⟨111⟩ surface is in contact with the liquid. There are 2688–3840

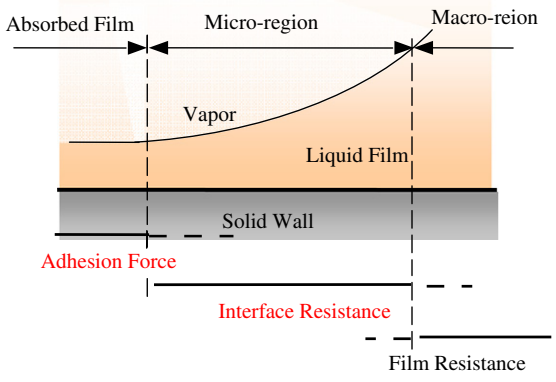

Fig. 1. Meniscus of the ultra-thin liquid film contact with the solid wall.

platinum atoms for the solid wall with nanostructures corresponding to its density of 21.45×10^3 kg/m^3. Fig. 3 shows the snapshots of the designed nanostructured surface and the definition of the size parameters, a, s, h and b. There are 6 cases of the nanostructured surface and the details of the parameters are listed in Table 1. For the nanostructured surfaces, the apparent solid surface with a distance of bh/s from the flat surface is applied corresponding to its size parameters as shown in Fig. 3(a)′. The liquid films in all simulations are performed in a state near saturation corresponding to the saturated density of 1.31×10^3 kg/m^3 of liquid argon at 100 K. If there is no wall effect, the flat nanochannel will be filled with 2400 atoms to achieve the saturated density at 100 K. Therefore, 1953–2400 argon atoms are prepared for the simulation cases corresponding to the spacing of the nanochannel composed of different nanostructured surfaces. For the simulations with the same nanostructured surface case, the liquid particle numbers of simulation cell (1) are the same as that of simulation cell (2).

For the intermolecular force field, the LJ potential is applied to argon with the length parameter $\sigma_l = 0.3405$ nm, and the energy parameter $\varepsilon_l = 1.67\times10^{-21}$ J as the liquid–liquid interaction. The LJ potential is also applied for the solid–solid interaction with $\sigma_s = 0.2475$ nm corresponding to the lattice constant 0.2776 nm of platinum, $\varepsilon_s = 8.35\times10^{-20}$ J for the potential well depth of Pt–Pt, taking no account of the electron contribution in Pt. For the solid–liquid interaction, a modified form of the LJ potential shown below is used:

$$\phi_{sl}(r_{ij}) = 4\alpha\varepsilon_{sl}\left[\left(\frac{\sigma_{sl}}{r_{ij}}\right)^{12} - \beta\left(\frac{\sigma_{sl}}{r_{ij}}\right)^{6}\right] \quad (1)$$

where $\sigma_{sl} = (\sigma_l+\sigma_s)/2$, and the energy parameter ε_{sl} is given by $\varepsilon_{sl} = \sqrt{\varepsilon_l\varepsilon_s}$ based on the Lorentz–Berthelot combining rule. Factors α and β of Eq. (1) are used to adjust the strength of molecular interaction with the responding values of the contact angle taken from previous simulations [15,16]. In this paper, we set α to the constant of $\alpha = \sqrt{\varepsilon_l/\varepsilon_s} = 0.14$, and set β to $\beta=1$ and $\beta=0.5$ respectively. For the flat surface, the hydrophilic characteristic (contact angle is zero) has been reported with the use of $\beta=1$. The contact angle of $\beta=0.5$ at the flat surface has been reported of 60°. Also, the nanoscale unevenness of the solid surface is an important

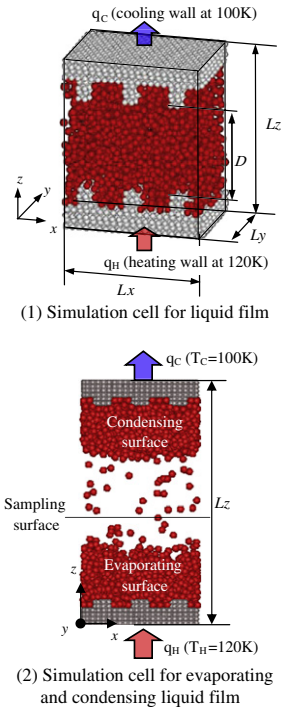

Fig. 2. Molecular dynamics simulation systems.

factor to the solid–liquid interface structure [5]. Simulation cases (a)–(g) are carried out with both the potential parameter $\beta = 1$ and $\beta = 0.5$.

All simulations are performed with a time step of 5fs and a selected cut off radius of $3.5\sigma_l$ for the spherically truncated and shifted (STS) potential. The equations of motion are integrated by the Velocity Verlet algorithm. After achieving a steady state from the initial state, the equilibrium system (without thermostat) at 100 K is simulated. Then, the non-equilibrium molecular dynamic simulation (NEMD) is carried out from the equilibrium state. In all NEMD simulations, the local data of liquid density are collected by 80 bins in the z direction and the segmental width of each bin was set to be 0.676 Å ($\approx \sigma_l/5$). Basically, the solid–liquid interface in atomic scale is the plane that divides the solid atoms and the liquid ones. However, the property (i.e. density) of liquid varies in a region of transition from the contacting layer upon the solid to the bulk liquid. Therefore, the solid–liquid interface also could be defined as a region of transition with an atomic scale thickness parallel to the solid surface. Since the apparent solid surface for the nanostructured surface locates at a distance of bh/s from the flat surface as shown in Fig. 3, the first layer of liquid at the solid–liquid interface can be located at the position of $(bh/s) + \sigma_l$ from the first layer of solid approximately. Therefore, the segmental width of each bin for data sampling of temperature and pressure in z direction is set to $2\sigma_l$ ($\approx$0.676 nm). Accordingly, the temperature and pressure profiles of liquid are collected by 8 bins in the z directions and the segmental width of each bin is set to be 0.676 nm. The local temperature T of each bin can be obtained from:

$$T = \frac{1}{N}\sum_{n=1}^{N}\frac{2}{3k_B}\sum_{i=1}^{3}\frac{1}{2}m\left(v_{n,i} - \bar{v}_i\right)^2 \tag{2}$$

where N is the particle number in the bin, k_B is the Boltzmann constant, m is the mass of the liquid particle, $v_{n,i}$ is the velocity of particle n in the i (=x,y,z) direction, and $\bar{v}_i$ is the mean velocity of the macro flow in the bin. In order to obtain realistic temperature distribution, no thermostat is coupled directly to the liquid particles and temperature control is only performed to the outside solid layers of the nanochannel. The heat flux passing through the steady non-equilibrium system is obtained from the heating and cooling energy of the thermostat based on the law of the energy conservation. Then, the thermal conductivity is calculated from the heat flux and temperature gradient.

$$\lambda = \frac{q}{\mathrm{d}T/\mathrm{d}z} \tag{3}$$

where $\mathrm{d}T/\mathrm{d}z$ is the local temperature gradient and it is almost constant for the bulk liquid. The thermal resistance at the solid–liquid interface is obtained from the heat flux and the temperature jump as shown in Eq. (4).

$$R_i = \frac{\Delta T}{q} \tag{4}$$

Here, ΔT is the temperature difference between the first liquid layer linked to solid and the first solid layer linked to liquid. It should be noted that the position of the first solid layer for the nanostrctured surfaces is generalized with the length of bh/s. Thus, the local temperature of the first liquid layer is estimated based on the temperature profile corresponding to the apparent surface height bh/s. Furthermore, the local pressure P of each bin is calculated according to the virial theorem;

$$P = \frac{Nk_BT}{V} - \frac{1}{6V}\sum_{i=1}\sum_{\substack{j>1\\ i\neq j}} r_{ij}\frac{\mathrm{d}\phi(r_{ij})}{\mathrm{d}r_{ij}} \tag{5}$$

where V is the volume of the bin. The first term in the right side is for the momentum flux caused by the molecular motion while the second term is for the contribution of the intermolecular forces. Long-range corrections are applied for the calculation of the pressure.

3. Results of simulation cell (1): liquid film in steady NEMD

As shown in Fig. 2, simulation cell (1) contains two solid–liquid interfaces subjecting to heating and cooling respectively (liquid film without phase change). 5 ns are used for the data sampling in a steady state under the non-equilibrium condition.

Fig. 4 shows the density, temperature and pressure profiles of the liquid film for the hydrophilic surfaces on the left side and the hydrophobic surfaces on the right side. The shadows illustrate the flat walls as a guide for eye. Due to the small scale of the separate distance of the walls, the effect of wall adsorption on the bulk density of the liquid is prominent for the hydrophilic surfaces. The mean density of the bulk liquid in cases (b)–(g) approximates to 1.21×10^{-3} kg/m^3 and it is lower than that of the bulk liquid for the flat surface 1.29×10^{-3} kg/m^3 as shown in Table 2. For the hydrophobic surfaces, the mean density of bulk liquid varies in a range of 1.31×10^{-3} kg/m^3 to 1.35×10^{-3} kg/m^3. Although the effect of wall adsorption is weakened at the hydrophobic surfaces, in most cases, the bulk liquid density of the nanostructured surface is lower than that obtained at the flat surface. This implies that the surface adsorption is improved at the nanostructured surfaces compared to the flat surface. Based on the density profile shown in Fig. 4, several ordering molecular layers can be found at the solid–liquid interface (i.e. the transition region from the adsorbed liquid to bulk liquid). The ordering molecular layers are also described as the solid-like liquid because they behave like liquid crystals [17,18]. It is found that the solid-like liquid structure at the nanostructured surface is

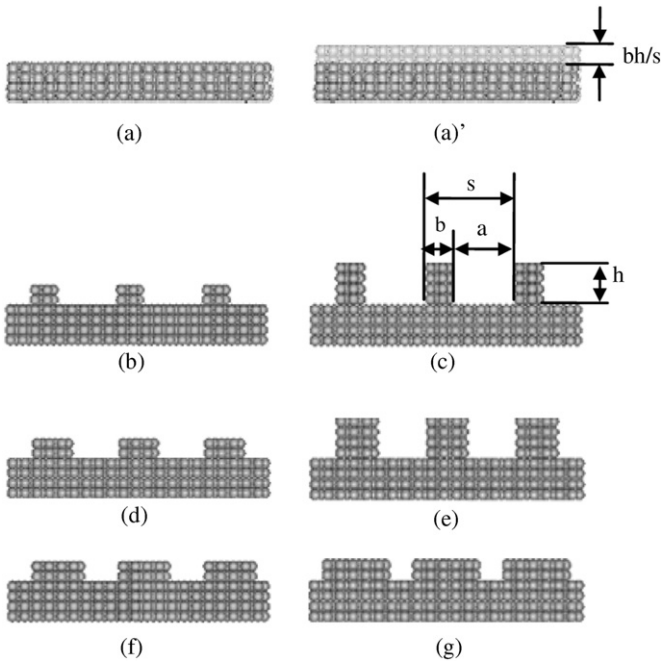

Fig. 3. Simulation cases of solid surface: (a) flat surface; (b)–(g) nanostructured surfaces; (a)′ apparent position of solid surface for nanostructured surfaces.

modified by the shape of the nanostructures and its first peak of the density is reduced in cases (b)–(g) compared to case (a).

The ordering liquid layers exhibit different behavior from its bulk not only in terms of density but also in terms of temperature and pressure. It is found that the pressure distribution of the nanostructured surface has a different shape compared to that of the flat surface in both the hydrophilic case and the hydrophobic case. The pressure of bulk liquid is almost uniform; however, the pressure in the adsorption layers adjacent to the nanostructured surfaces is lower than the bulk pressure in most cases. The molecular adsorption is considered to be the main reason of the local low pressure as a result of the solid–liquid interface disjoining pressure.

As shown in Fig. 4, the temperature distribution shows the difference between the hydrophilic case and the hydrophobic case. The mean temperature of the bulk liquid is near 110 K in all simulation cases. Apparent temperature jumps can be found in the vicinity of the solid surfaces. It is clear that the temperature jump at the hydrophilic surfaces is smaller than that of the hydrophobic surfaces. The details of the temperature jumps and the local heat flux collected at the heating surface (ΔT_H, q_H) and cooling surface (ΔT_C, q_C) in all cases are summarized in Table 2. We can find an equivalent amount of the heat flux at the heating surface and the cooling surface for all simulation cases; thus, it could be supposed that the simulation system is in a steady state. Obviously, simulation cases (b)–(g) have a larger amount of heat flux than case (a) at both the hydrophilic and hydrophobic surfaces. The heat flux of the hydrophilic surface (107.0 MW/m^2) is about 4.2 times to that of the hydrophobic surface (25.2 MW/m^2) for the flat cases; however, the ratios decrease to 2.6–3.4 for the nanostructure cases.

Since the surface area increases with increasing the nanostructures, the parameter r_w is used to describe the area ratio of the nanostructured surface to the flat surface. The heat flux versus the surface area ratio r_w is plotted in Fig. 5. As shown in Fig. 5, the heat flux increases with increasing the surface area ratio r_w at both the hydrophilic and hydrophobic interfaces. It can be seen that the rate of heat flux increase caused by nanostructures effects are almost in proportion to the surface area increment at the hydrophobic surface and the hydrophilic surface. The hydrophilic cases show less effect of increasing surface area and the maximum of heat flux is about 1.5 times larger than that of the flat surface when r_w is 1.97. For the hydrophobic cases, the maximum of heat flux is about 2.3 times larger than that of the flat surface. The heat flux increase at the nanostructured surface is not monotonously dependent on the area increment strictly. It is slightly affected by the sizes of the nanostructures. Also, the thermal conductivity at the solid–liquid interface obtained from the heat flux and the temperature gradient are shown in Table 2. It is found the thermal conductivity at nanostructured surface is higher than that of the flat surface and thus, lower thermal resistance is obtained.

Table 1
Parameters and simulation cases.

Cases	Nanostructure parameters [nm] ($s = a + b = 1.943$)			Apparent surface [nm]	Surface area ratio [–]	θ [$\pm 5^\circ$] ($\alpha = 0.14$)	
	a	b	h	bh/s	$r_w = (s + 2h)/s$	$\beta = 1$	$\beta = 0.5$
(a)	–	–	–	0	1.000	0	60
(b)	1.388	0.555	0.453	0.129	1.467	0	87.3
(c)	1.388	0.555	0.907	0.259	1.933	0	85.5
(d)	1.110	0.833	0.453	0.195	1.467	0	86.9
(e)	1.110	0.833	0.907	0.389	1.933	0	95.1
(f)	0.833	1.110	0.453	0.259	1.467	0	86.2
(g)	0.555	1.388	0.453	0.324	1.467	0	84.9

4. Results of simulation cell (2): evaporating liquid film in unsteady NEMD

For simulation cell (2) of liquid film with phase change, two liquid–vapor interfaces subjected to evaporation and condensation respectively are prepared in addition to two solid–liquid interfaces as shown in Fig. 2. The NEMD simulation is started in an initial state of the same film thickness of about 2.7 nm ($\approx 8\sigma_l$) at the evaporating surface and the condensing surface. In this paper, we only focus on the continuous liquid films on the hydrophilic surfaces

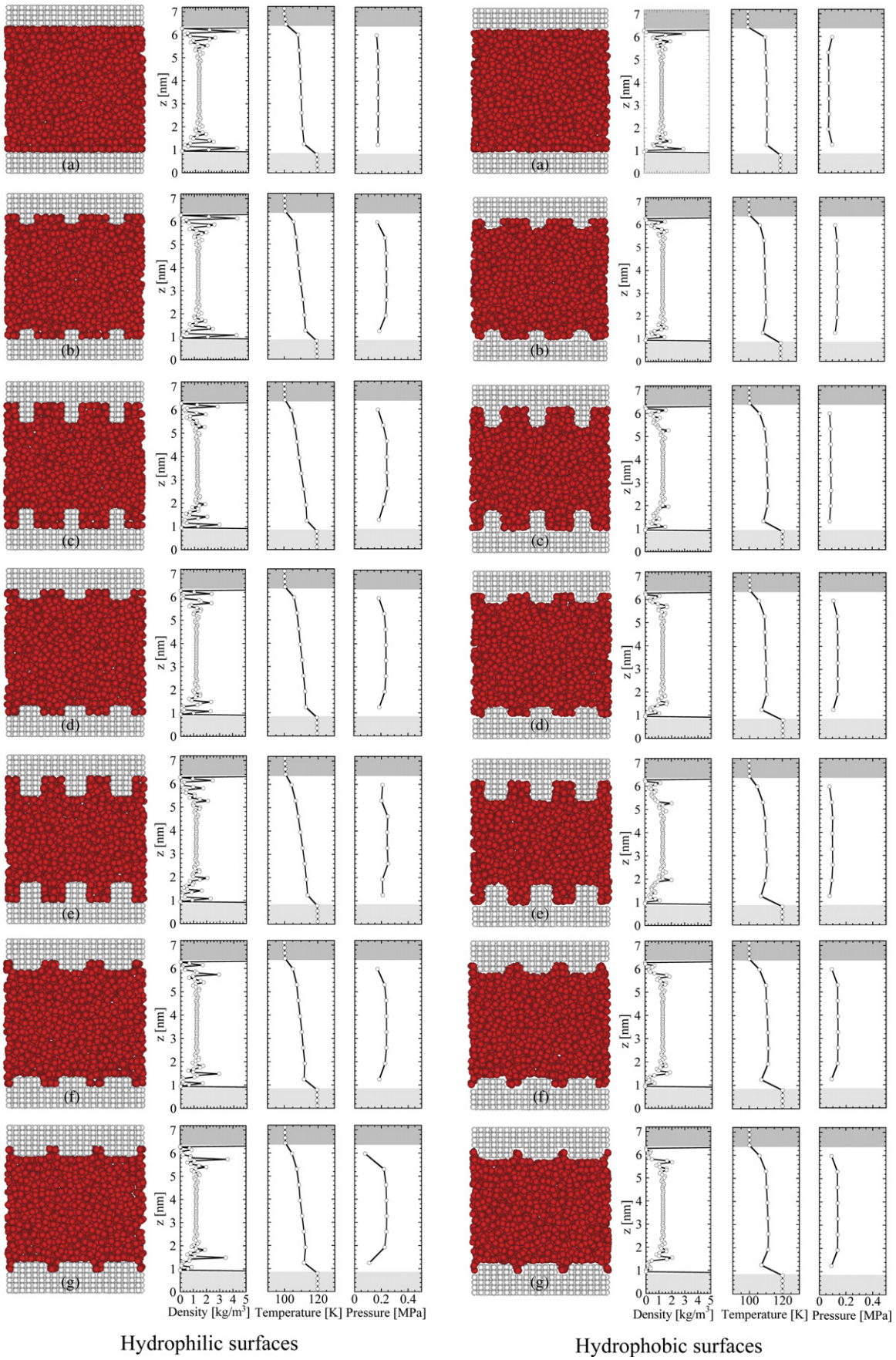

Fig. 4. Density, temperature and pressure profiles of liquid film in the simulation cell (1) for the hydrophilic surfaces (left) and hydrophobic surfaces (right). The shadows illustrate the flat walls.

Table 2
Simulation results of the liquid film in the steady non-equilibrium system.

Cases	$\overline{\rho_l} \times 10^{-3}$ [kg/m^3]	ΔT [K]		q [MW/m^2]			λ [W/m K]		$R_i \times 10^{-7}$ [m^2 K/W]	
		ΔT_H	ΔT_C	q_H	q_C	$\overline{q}$	λ_{iH}	λ_{iC}	R_{iH}	R_{iC}
Hydrophilic surface ($\alpha = 0.14$, $\beta = 1.0$)										
Flat	1.29	9.08	8.83	105.7	102.3	104.0	0.013	0.013	0.779	0.810
(a)	1.21	7.77	7.16	134.9	136.2	135.6	0.018	0.019	0.461	0.416
(b)	1.21	6.86	6.55	162.6	160.7	161.7	0.024	0.025	0.302	0.283
(c)	1.21	7.49	7.63	128.3	127.1	127.7	0.017	0.017	0.472	0.483
(d)	1.21	6.98	6.56	151.5	151.9	151.7	0.022	0.023	0.332	0.305
(e)	1.21	7.68	7.51	124.5	123.4	124.0	0.016	0.017	0.503	0.489
(f)	1.21	7.48	7.33	136.1	134.0	135.1	0.018	0.019	0.439	0.427
Hydrophobic surface ($\alpha = 0.14$, $\beta = 0.5$)										
Flat	1.35	8.30	10.98	24.5	26.0	25.2	0.003	0.002	3.206	4.269
(a)	1.32	9.08	9.59	40.8	39.7	40.3	0.004	0.004	2.156	2.283
(b)	1.35	9.10	9.35	56.9	56.2	56.6	0.006	0.006	1.526	1.570
(c)	1.32	9.84	8.97	40.9	40.2	40.5	0.004	0.005	2.340	2.125
(d)	1.35	10.05	8.38	59.1	58.0	58.6	0.006	0.007	1.636	1.353
(e)	1.31	8.78	9.94	44.5	47.2	45.9	0.005	0.005	1.831	2.083
(f)	1.32	10.10	9.22	38.1	37.9	38.0	0.004	0.004	2.603	2.371

with the parameter $\alpha = 0.14$, $\beta = 1.0$ because the liquid film is discontinuous in the hydrophobic cases when the evaporation proceeds. A surface located in the vapor region sandwiched by the liquid film shown in Fig. 2 is used for data sampling to obtain the net evaporation molecular number from the evaporating surface to the condensing surface and the evaporation rate.

The evaporation behaviors of the ultra-thin liquid film at the nanostructured surfaces (b)–(g) are similar to each other. Fig. 6 shows the examples of the evaporation process of the liquid film at the surfaces (f) and (g). It is found that the film thickness of the evaporating surface decreases during the period of $t = 0$–3 ns rapidly and then the system reaches a steady state when the film thickness keeps almost constant. Obviously, the adsorbed layer of non-evaporation exists at the solid–liquid interface due to the hydrophilic intermolecular force field.

Fig. 7 shows the snapshots of the liquid film at the flat surface and the nanostructured surfaces at $t = 5$ ns after NEMD starting. Although the liquid film on the flat surface becomes much thinner than its initial state, it is thicker than those of the nanostructured cases (b)–(g). The evaporation of the liquid film on the flat surface lasts 3 ns longer and the system reaches a steady state at $t = 8$ ns. This means that the liquid film evaporates faster at the nanostructured surfaces than the flat surface. The reason is that the solid–liquid interface resistance for the nanostructured surfaces is lower than that of the flat surface (shown in Table 2). Also, it is found that the non-evaporation layer exists in all cases.

Fig. 8 plots the data collected at the vapor region of the net evaporation molecular number during the simulation period of $t = 0$–6.8 ns. The number of evaporation molecules increases as the simulation time proceeds and the evaporation rates could be obtained based on the data of Fig. 7. It is found that the evaporation rates of nanostructured surfaces during the period of $t = 0$–2 ns is almost constant and the mean value of about 827.87 kg/m^2 s is obtained. This means that the evaporation phenomena are dominated by the liquid–vapor interface and the nanostructures show less effect on the evaporation rate. After $t = 2$ ns, the evaporation rate decreases rapidly because the liquid–vapor interface is affected by the solid–liquid interaction. The liquid particles are restricted to the absorbed layer and the evaporation rate is decreased to 0 after $t = 5$ ns. On the other hand, the mean evaporation rate during $t = 0$–6 ns is about 466.17 kg/m^2 s on the flat surface, which is much lower than that of the nanostructured surface. It shows that the evaporation rate for the nanostructured surface decreases earlier than that for the flat surface (2 ns compared with 6 ns for the flat surface). This implies that the nanostructures can enhance the evaporation through ultra-thin liquid film since the thermal resistance at the solid–liquid interface can be reduced by the nanostructures.

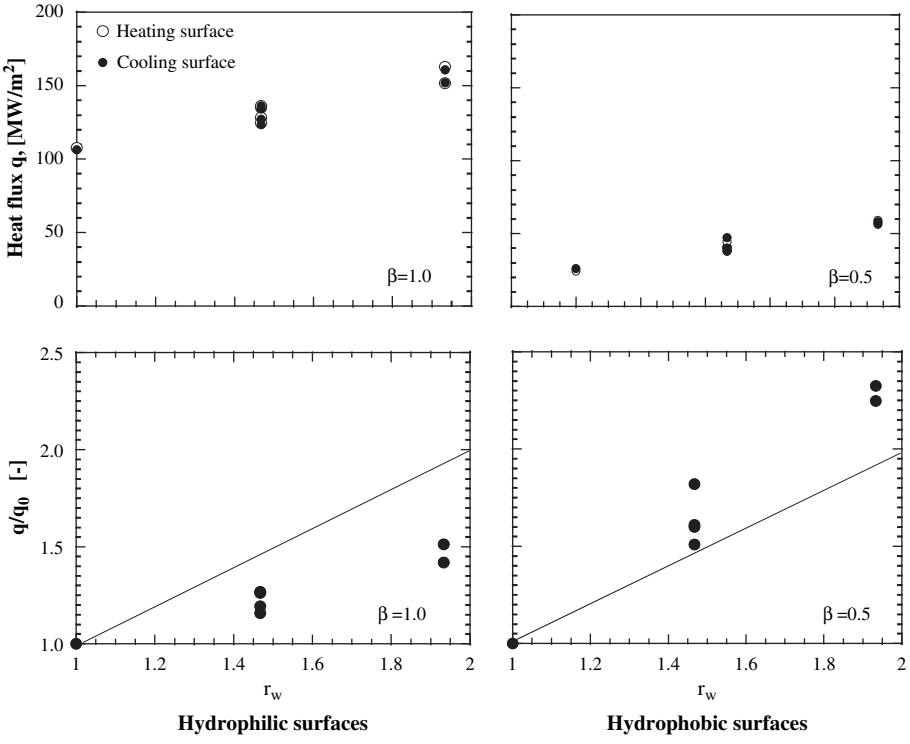

Fig. 5. Heat flux versus surface area ratio (q_0 is the heat flux of flat surface). The lines are guide for eye.

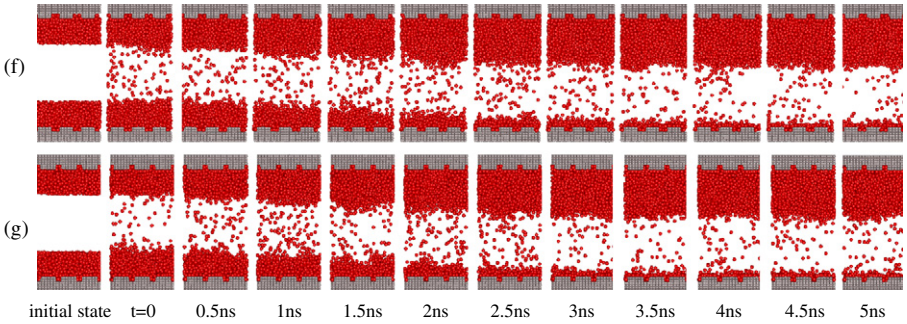

Fig. 6. Evaporation process during 5 ns of the ultra-thin liquid film at the nanostructured surface (snapshot examples of simulation cases (f) and (g)).

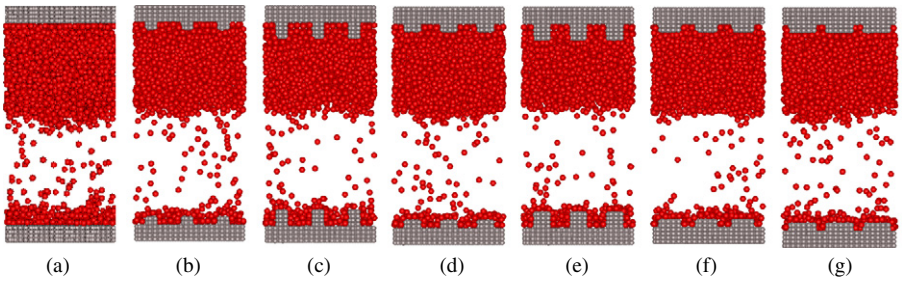

Fig. 7. Comparisons of the ultra-thin liquid films after 5 ns from evaporation starting.

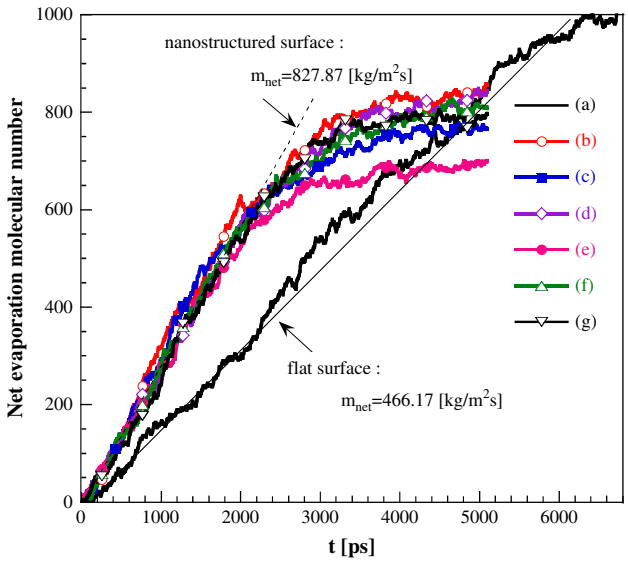

Fig. 8. Net evaporation molecular number and evaporation rate of the ultra-thin liquid film at the nanostructured surfaces (b)–(g) in comparison with that of the flat surface.

5. Conclusions

Molecular dynamics simulations of the interfacial heat and mass transfer for ultra-thin liquid film at nanostructured surface have been carried out and the following conclusions may be drawn from the present study:

(1) Thermal resistance at the solid–liquid interface can be reduced by the nanostructures located in the interface zone. Significant heat transfer enhancement can be achieved at the nanostructured surface compared to the flat surface due to the area increment of the solid–liquid interface.

(2) The effect of surface nanostructure is important in determining the evaporation rate of the ultra-thin liquid film. The evaporation rate at the hydrophilic nanostructured surface has the larger value than that of the flat surface when the film thickness is larger than that of the adsorbed layer.

Acknowledgments

This work is partly supported by the Ministry of Education, Science and Culture of the Japanese Government through the Grant-in Aid for Scientific Research, Project No. 19560207 and No. 21360099, the research grant from the Mazda Foundation and the research supercomputing services by the Research Institute for Information Technology of Kyushu University.

References

[1] R. Blossey, Self-cleaning surfaces – virtual realities, Nature Materials 2 (2003) 301–306.
[2] N. Moronuki, et al., Design of surface texture of the control of wettability, Transactions of the Japan Society of Mechanical Engineers B 70 (693) (2004) 1244–1249.
[3] K. Takahashi, Porous silicon as a superhydrophobic microchannel surface, in: Proceedings of the First ISMNT, 2004, No. XXX I-2-03.
[4] E. Hosono, et al., Superhydrophobic perpendicular nanopin film by the bottom-up process, Journal of the American Chemical Society 127 (39) (2005) 13458–13459.
[5] G. Nagayama, S. Shi-iki, T. Tsuruta, Effects of naostructures on surface wettability: a molecular dynamics study, Transactions of the Japan Society of Mechanical Engineers B 73 (728) (2007) 1084–1091.
[6] T. Kunugi, Heat transfer enhancement by nano-scale structure formed on surface: experimental and molecular dynamics study, in: Proceedings of the First ISMNT, 2004, No. XXV II-3-01.
[7] T. Kunugi, K. Muko, New Heat-Exchange and Heat-transfer Methods between Solids and Fluids, Patent# 2002-297088, JP.
[8] G. Nagayama, M. Kawagoe, T. Tsuruta, Molecular dynamics simulations of interfacial heat and mass transfer at nanostructured surface, in: Proceedings of the MNC2007-21410, 2007, pp. 1–10.
[9] S. Maruyama, T. Kimura, A study on thermal resistance over a solid–liquid interface by the molecular dynamics method, Thermal Science & Engineering 7 (1) (1999) 63–68.

[10] P. Yi, D. Poulikakos, J. Walther, G. Yadigaroglu, Molecular dynamics simulation of vaporization of an ultra-thin liquid argon layer on a surface, International Journal of Heat and Mass Transfer 45 (2002) 2087–2100.
[11] C.Y. Ji, T. Tsuruta, G. Nagayama, Effects of solid heating surfaces on nanometer-sized liquid films, Thermal Science & Engineering 13 (24) (2005) 25–28.
[12] R. Khare, P. Keblinski, A. Yethiraj, Molecular dynamics simulations of heat and momentum transfer at a solid–fluid interface: relationship between thermal and velocity slip, International Journal of Heat and Mass Transfer 49 (2006) 3401.
[13] T. Ohara, D. Torii, Molecular thermal phenomena in an ultrathin lubrication liquid film of linear molecules between solid surfaces, Microscale Thermophysical Engineering 9 (2005) 265.
[14] T. Ohara, D. Torii, Molecular dynamics study of thermal phenomena in an ultrathin liquid film sheared between solid surfaces: the influence of the crystal plane on energy and momentum transfer at solid–liquid interfaces, The Journal of Chemical Physics 122 (2005) 214717.
[15] G. Nagayama, P. Cheng, Effects of interface wettability on microscale flow by molecular dynamics simulation, International Journal of Heat and Mass Transfer 47 (2004) 501–513.
[16] G. Nagayama, T. Tsuruta, P. Cheng, Molecular dynamics simulation on bubble formation in a nanochannel, International Journal of Heat and Mass Transfer 49 (2006) 4437–4443.
[17] S. Somers, H.T. Davis, Microscopic dynamics of fluids confined between smooth and atomically structured solid surface, Journal of Chemical Physics 96 (7) (1992) 5389–5407.
[18] I. Bitsanis, J.J. Magda, M. Tirrell, H.T. Davis, Molecular dynamics of flow in microscopes, Journal of Chemical Physics 87 (3) (1987) 1733–1750.